RESSAC: A New Airborne FM/CW Radar Ocean Wave Spectrometer

Danièle Hauser, Gérard Caudal, Gert-Jan Rijckenberg, Daniel Vidal-Madjar, Georges Laurent, Philippe Lancelin

***Abstract*— We present the French radar system RESSAC, used from aircraft platforms for measuring directional spectra of ocean waves in the gravity domain (wavelengths from 30 to 400 m). The instrument consists of a *C*-band (5.35 GHz) FM/CW radar system. The transmitting and receiving antennas are looking toward the surface at a low incidence angle ($\approx 14°$ for the center of the antenna beam), and rotate around a vertical axis. When processing the data, one removes the known antenna gain pattern from the recorded signal, thus making it possible to estimate the sea surface slope variance, which in turn is used to determine the tilt modulation transfer function, without the need of any external wind measurement. Fully normalized spectra obtained from RESSAC are presented and compared to other data sets (nondirectional frequency spectra from buoy measurements, directional spectra from a ship radar and from a sea-state model). The consistency is in general very satisfactory, and the estimates of sea surface slope variance inferred from RESSAC are consistent with the wind observations and with previous results found in the literature.**

I. Introduction

OUR ability to progress in the understanding of the physics of wind-generated ocean waves and to improve the modeling and prediction of sea-state is obviously related to the development of extensive and good quality measurements of the sea surface.

The available instruments designed as tools for the measurement of sea-surface waves can be classified according to three different types: buoy systems, optical techniques, and radar systems.

Accelerometer buoys (measuring heave as a function of time) are currently used to provide spectra of sea-surface waves in terms of spectral energy density as a function of the wave frequency. Directional buoys (measuring heave, roll, and pitch as a function of time) can provide in addition an estimate of the first two terms of the angular distribution of the spectral components. However, the directional resolution obtained with these systems is relatively coarse, and the periods of sampling are too short to obtain the spectral amplitudes with a good accuracy [1]. Moreover, any buoy system provides only local information and is difficult to moor outside coastal areas.

The operational use of optical techniques is difficult, due to the fact that they can only be operated during favorable atmospheric conditions and require intensive processing.

Manuscript received February 25, 1991; revised October 21, 1991; rerevised January 20, 1992.

The authors are with Centre de Recherches en Physique de l'Environnement Terrestre et Planétaire (CRPE), CNET/CNRS, 38 Rue du Général Leclerc, 92131-Issy-les-Moulineaux, France, except G.-J. Rijckenberg, who is now with Landbouw Universiteit, Wageningen, The Netherlands.

IEEE Log Number 9200751.

These difficulties and the interest in mesoscale or global scale measurements of sea-state has favored the development of radar systems either in the HF domain [2], [3] or in the microwave domain (see [4]–[7] for a review of these systems). The microwave sensors have been studied more frequently because they have the advantage of being usable from aircraft and (for some of them) from space platforms.

As a matter of fact, the only radar system implemented on spacecraft for measuring ocean wave spectra, is the synthetic aperture radar (SAR). It has been used since 1978 (Seasat, SIR-B) to derive ocean wave spectra from space [8]–[13], and a number of projects are planned for the future. In particular the European oceanographic satellite ERS-1 (launched in July 1991) carries a SAR which is used to image the surface. However the quantitative interpretation and the use of the information provided by the SAR images is still a subject of study [14]–[16], because the relationship between the ocean wave spectra and the image spectra (i.e., the transfer function) is still not satisfactorily determined, and because a distortion of the SAR image may occur, in particular when the ocean waves travel in the same direction as the satellite track. Although this latter effect seems less dramatic when low-altitude spacecraft (as the space shuttle with SIR-B) are used [12], [17], there is still a great need for research to understand the backscatter mechanisms of centimetric electromagnetic waves from the ocean surface, and to validate the theory built to interpret the SAR images.

In this context, several airborne microwave sensors operating without the constraints of synthetic aperture radars have been developed: the Surface Contour Radar (SCR) developed by Walsh *et al.* [18]–[19] and the Radar Ocean Wave Spectrometer (ROWS) developed by Jackson *et al.* [20]–[22] are the more widely used radar-systems for the measurement of ocean-wave spectra from aircraft.

In Europe, the European Space Agency (ESA) and the French Space Agency (CNES) supported a new airborne radar project, call "RESSAC" (Radar pour l'Etude du Spectre des Surfaces par Analyse Circulaire), whose first aim is to serve as a tool for the geophysical validation of the ERS-1 wave measurements. In the present paper, we present this new system, which is based upon the same principle of measurement as the ROWS developed by Jackson [21], [22], i.e., analysis of the reflectivity modulation due to the tilt of the long waves (wavelength larger than 30 m), and observed from low-incidence angle measurements. Compared to the American ROWS, RESSAC has the advantage of its lower cost and lower power requirements, due to the choice of the Frequency

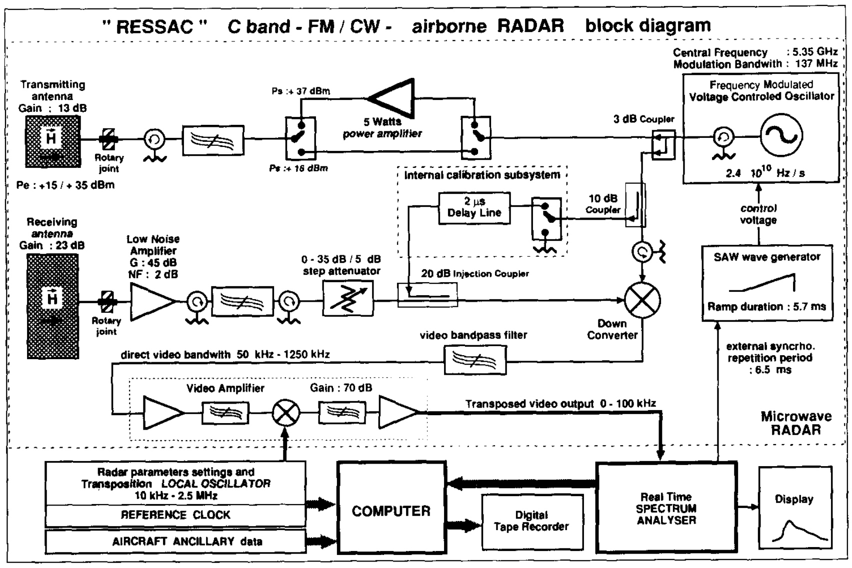

Fig. 1. Block diagram of the radar RESSAC.

Modulated/Continuous Wave technique. It has been built by adapting an airborne scatterometer developed in France for remote sensing over land surfaces [23]. Until now, RESSAC has only been involved in two limited experiments, but the first set of results described in this paper are encouraging. The characteristics of the system are described in Section II. Section III recalls the principle of the measurement, and presents the improvements relative to the method proposed by Jackson *et al.* [21], [22]. The detailed data processing method is given in Section IV, and results are discussed in Section V.

II. The RESSAC System

The RESSAC system consists of a *C*-band FM/CW (Frequency-modulated Continuous Wave) radar whose block diagram is shown in Fig. 1, and whose characteristics are summarized in Table I. The radar has been developed at our laboratory, and is derived from the airborne scatterometer ERASME, which was designed as a research tool for remote sensing applications [23]. The characteristics of the RESSAC system have been chosen so as to optimize the ability of the instrument to measure ocean wave two-dimensional spectra. The radar can be mounted on two airplanes, either the Dornier 228 of DLR (Germany), or the Merlin-IV of Météo-France (France), whose flight speed is typically around 100 m/s. The transmitting and receiving antennas are looking at an angle of 14° from the nadir, and perform one rotation per minute around a vertical axis. The nominal flight altitude of RESSAC is usually chosen as 6000 m. In this condition, the lobes of the transmitting and receiving antennas (see Table I) are such that the beam spot on the sea surface has a half-power width of the order of 1500 m in the direction of the incidence plane (or elevation direction, hereafter denoted as the x-direction), and 375 m in the perpendicular direction (or azimuthal direction, or y-direction).

Following the principle of the FM/CW radar, a signal with linear frequency modulations is transmitted continuously with constant amplitude during a sweep time $T(= 5.71$ ms). Assuming a scattering object at distance R, the received signal is delayed by a time interval Δt proportional to R. The simultaneously transmitted and received signals (at frequencies f_t and f_r, respectively) are passed through a mixer and a low-pass filter, thus producing a beat signal, whose frequency is the difference frequency $f_t - f_r$ (or beat frequency), and is proportional to distance R. A spectrum analyzer performs a FFT on the beat signal received from each modulation ramp (every 6.5 ms), yielding a power spectrum. A time integration is performed on the power spectra. The number of integrated samples can be chosen as $N = 4$, 8, 16, or 32. Usually $N = 32$ is chosen, which yields one integrated spectrum every 0.2 s, which is recorded on a digital tape for further processing. The time, as well as the aircraft flight parameters (pitch, roll, heading, velocity, drift, latitude, longitude, ...) are included within each record containing a radar spectrum (every 0.2 s in the nominal mode).

The distance resolution δR is related to the frequency resolution of the radar spectrum δf (= 250 Hz) through: $\delta R = (c/2\mu)\delta f$, where $\mu(= 2.4 \times 10^{10}\text{Hz/s})$ is the frequency sweep rate of the frequency modulation ramp, and c is the velocity of light. This yields: $\delta R = 1.56$m. In fact, due to the FFT analysis procedure used, contiguous frequency points are not independent. The width of the impulse response of the analyzer is of the order of $1.74\delta R$. Only 400 frequency points are recorded on tape, which thus correspond to a total analyzed band of 100 kHz, and cover a distance of 624 m. Through an adjustable local oscillator, the analyzed band is chosen so that the first recorded sample be at a distance slightly less than the aircraft altitude, so as to get the useful part of the power profile. The total dynamic range of the received signal is about 40 dB. A set of attenuators (from 5 to 25 dB with 5-dB steps)

TABLE I
RESSAC RADAR CHARACTERISTICS

Type	FM-CW	
Mean frequency	5.35 GHz (C-band)	
Transmitted power	32 mW (15 dBm) or 3400 mW (35.3 dBm)	
Receiver	Total gain 93.5 dBV	
Modulation	Upward linear frequency modulation	
	Duration	5.71 ms
	Bandwidth	137 MHz
	Repetition period	6.5 ms
Antennas	Polarization HH	
	Mean incidence angle	14°
	Beam width (at 3 dB)	±6.5° in elevation
		±1.7° in azimuth
	Two-way gain	≈ 36 dB
	Rotation in azimuth	360° /minute
	Closest sidelobe (at mean frequency):	20 dB below maximum
		11° away from beam axis in azimuth
Signal Processing	FFT Analyzer, 512 points (400 retained)	
	Adjustable analyzed band of 100 kHz width	
	Resolution	250 Hz in frequency
		1.56 m in range
	Number of integrations	4, 8, 16, or 32
	Digitalyzed output with a 0.1 dB sensitivity	
Ancillary data	Clock, antennas rotation angle,	
	Flight parameters (pitch, roll, heading, speed...) from the NIS through ARINC output protocole	

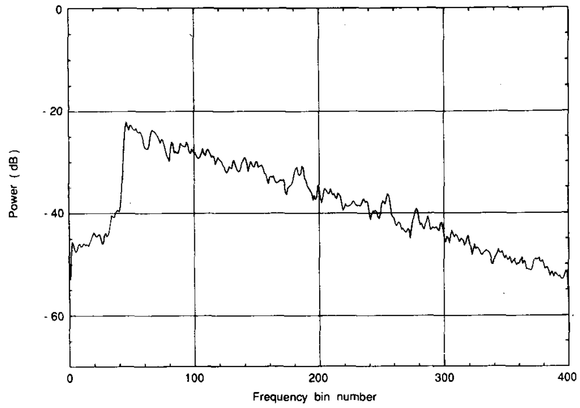

Fig. 2. Example of a power spectrum recorded on-board by the RESSAC system. The horizontal axis is labeled by the frequency bin number, from 1 to 400. The frequency interval between two consecutive bins is 250 Hz, corresponding to a distance interval of 1.56 m.

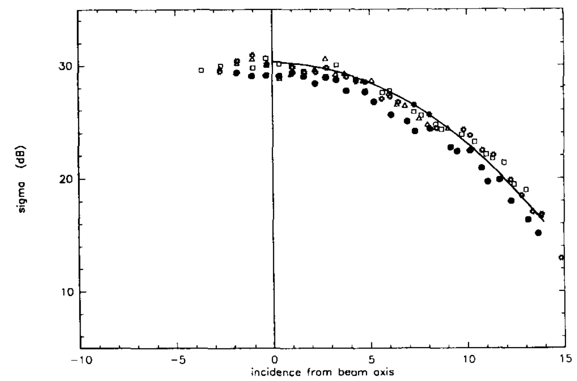

Fig. 3. Antenna lobe pattern in elevation as inferred from measurements during a flight over corner reflectors (four different symbols for each reflector). The solid curve corresponds to the Gaussian function which fits the laboratory measurements of the antenna lobe.

can be used to adjust the level of the signal within the dynamic range of the receiver. Fig. 2 shows a typical spectrum plotted as a function of the frequency bin (or equivalently the range bin within the plane of incidence). The sharp increase in the received power at bin 40, corresponds to the sea surface echo at nadir, even though the nadir is about 14° away from the antenna beam axis. The reason for it is that the antenna lobe pattern is relatively broad in elevation (±6.5° half power beam width in elevation), which is sufficient to give a sharp rise of the radar return at the nadir whatever the exact attitude of the aircraft is. At larger distances a gradual decrease of the power is observed.

The antenna lobe characteristics given in Table I are those deduced from measurements performed at the CNET facility at La Turbie (France). The measurements have shown that the transmitting and receiving gain functions can be approximated as Gaussian functions. In addition, test flights of RESSAC over a set of corner reflectors were performed, in order to evaluate the antenna lobe shape when mounted on the aircraft. Fig. 3 displays the results of one of the test flights, giving the received power as a function of incidence angle. The comparison with the Gaussian lobe model inferred from La Turbie is excellent, and gives confidence in the knowledge that we have of the antenna characteristics.

III. The Rows Principle

It has been shown by Jackson [20] that it is possible to measure the characteristics of the long ocean waves by means of an airborne real aperture radar which is looking at angles near the vertical, and rotating around a vertical axis. The principle of the measurement consists in relating the change in the backscattering cross-section of the ocean surface to the slope of the long ocean waves. Further observations performed with his ROWS [21], [22] confirmed his linear tilt model, which will be briefly reviewed here.

Near vertical incidence (incidence angle $\theta \leq 15°$), microwave backscatter from the sea surface occurs through quasi-specular reflections from wave facets oriented normal to the radar's line of sight. The radar cross-section is then given by (e.g., Valenzuela [24]):

$$\sigma^\circ(\theta,\phi) = \rho\pi \frac{p(\tan\theta, 0)}{\cos^4\theta} \tag{1}$$

where θ is the incidence angle from nadir, ϕ denotes the azimuthal direction, ρ is a diffraction-modified normal incidence Fresnel reflectivity [25], and $p(\tan\theta, 0)$ is the slope probability density function (pdf) of the wave components which are longer than the diffraction limit (about three times the electromagnetic wavelength [25]). The slope pdf is evaluated at specular condition, which corresponds to sea surface slopes $\partial\zeta/\partial x = \tan\theta$, $\partial\zeta/\partial y = 0$.

In the linear tilt model, Jackson neglects the hydrodynamic modulation, because it appears to be a second-order effect near vertical backscatter. The sea surface is then treated as a free wave superposition possessing Gaussian statistics, and the slopes of the long waves (wavelength $\Lambda \geq 30$m) are assumed to be small compared to the total rms surface slope (from the long waves down to the diffraction limit). If the tilt ε due to the long wave is small, then the fractional variation of the radar cross-section due to the tilt ε is (from (1)):

$$\frac{\delta\sigma^\circ}{\sigma^\circ} = \frac{\delta p(\tan\theta, 0)}{p(\tan\theta, 0)} - \frac{\delta(\cos^4\theta)}{(\cos^4\theta)}. \tag{2}$$

Provided that $\varepsilon \ll \theta$, the local incidence angle can be approximated by:

$$\theta' = \theta - \frac{\partial\zeta}{\partial x}. \tag{3}$$

Therefore, from (2):

$$\frac{\delta\sigma^\circ}{\sigma^\circ} = \left[-4\tan\theta - \frac{1}{\cos^2\theta}\frac{\partial(\ln p)}{\partial(\tan\theta)}\right]\cdot\left(\frac{\partial\zeta}{\partial x}\right). \tag{4}$$

This is slightly more accurate than eq. (5) of Jackson *et al.* [21], in which the term $(-4\tan\theta)$, as well as the factor $(1/\cos^2\theta)$ in the last term, were omitted.

The fractional reflectivity modulation at azimuth ϕ has been defined by Jackson *et al.* [21] as:

$$m(x,\phi) = \frac{\delta P_r}{P_r} \tag{5}$$

where P_r is the received power at range R corresponding to the horizontal distance x, and δP_r is the difference between the measured P_r and the value of P_r that would occur in the absence of long-wave tilt.

We introduce here a modified reflectivity modulation $m'(x,\phi)$:

$$m'(x,\phi) = m(x,\phi)\left[\cot\theta - 4\tan\theta - \frac{1}{\cos^2\theta}\frac{\partial(\ln p)}{\partial(\tan\theta)}\right]^{-1} \tag{6}$$

In (6), the bracket term is a normalization factor arising from the specular reflection model. Jackson *et al.* [21] did not try to estimate this term from the radar data, but used independent buoy measurements to estimate it. In our case, we propose a method (see below) to estimate this bracket term. This allows us to get normalized sea-wave spectra without using any external measurements.

The modulation spectrum $P'_m(K,\phi)$ is taken as the spectrum of $m'(x,\phi)$, namely,

$$P'_m(K,\phi) = (2\pi)^{-1}\int_{-\infty}^{+\infty}\langle m'(x,\phi)\cdot m'(x+\xi,\phi)\rangle e^{-iK\xi}d\xi. \tag{7}$$

Let us now assume a Gaussian azimuthal antenna lobe pattern $G_t(y)\cdot G_r(y) = \exp(-y^2/L_y^2)$. One can then show that in the limiting case of a footprint with a very large azimuthal width ($KL_y \gg 1$), one gets:

$$P'_m(K,\phi) = \frac{\sqrt{2\pi}}{L_y}K^2F(K,\phi). \tag{8}$$

In this case of a large azimuth footprint, the directional resolution $\delta\phi$ is given by [21]:

$$\delta\phi \approx \frac{\delta K_y}{K} = 2\sqrt{2\ln 2}\left[(KL_y)^{-2} + (L_y\cot\theta/2H)^2\right]^{1/2}. \tag{9}$$

where H is the altitude.

In practice, the use of the hypothesis of a large azimuth footprint will limit the validity of our measurements to wavelengths smaller than ≈ 400 m, which is the azimuthal width of the beam spot on the sea surface.

If the slope probability distribution function (pdf) is Gaussian and is denoted $p(\partial\zeta/\partial x, \partial\zeta/\partial y)$, then:

$$p(\tan\theta, 0) = \frac{1}{2\pi\sigma_u\sigma_c}\exp\left(-\frac{\tan^2\theta}{v}\right) \tag{10}$$

where the parameter v is related to the upwind and crosswind slope variances σ_u^2 and σ_c^2 through:

$$v = 2\left[\frac{\cos^2\phi_1}{\sigma_u^2} + \frac{\sin^2\phi_1}{\sigma_c^2}\right]^{-1} \tag{11}$$

in which ϕ_1 is the angle between the look direction and the upwind direction. If the slope pdf were further isotropic, then v would not depend on the look direction and would be equal to $2\langle(\partial\zeta/\partial x)^2\rangle = \langle|\nabla\zeta|^2\rangle$.

Assuming a Gaussian (but not necessarily isotropic) slope pdf, one can write (6) as:

$$m'(x,\phi) = m(x,\phi)\cdot\left[\cot\theta - 4\tan\theta + \frac{2}{v\cos^2\theta}\tan\theta\right]^{-1}. \tag{12}$$

From (7), (8), and (12), one can see that the retrieval of the sea wave two-dimensional slope spectrum from the radar modulation spectrum requires the knowledge of the slope variance v. Jackson *et al.* [22] have shown how this parameter can be inferred from external buoy measurements of the wind speed. In the next section we shall outline the procedure that we use to analyze the RESSAC data, in which we determine v routinely from the radar returns themselves, without the need of any external measurement of the wind.

IV. Data Processing

The data processing consists in calculating the ocean wave height spectra, or wave slope spectra along the aircraft ground track, from the raw data recorded on tapes.

The processing is achieved through eight successive steps listed hereafter, and described in details in the following subsections: (A) altitude determination, (B) geometric corrections to take into account the aircraft attitude (roll, pitch) and to determine the gain value associated to each sampled point, (C) determination of the modulation function $m(x, \phi)$ (D) determination of the sea surface slope v and of the modulation function m', (E) Determination of the modulation spectrum (F) Determination of the sea surface height or slope spectrum, after corrections due to speckle, broadening of the impulse response function of the radar, and footprint displacement within the sampling time interval, (G) averaging procedures, (H) determination of physical useful quantities.

The output of this processing consists of averaged wave slope spectra given as a function of 64 wave numbers $K(4 \times 10^{-3} \leq K \leq 2.56 \times 10^{-1}\text{cpm})$ and 72 azimuth angles (5° interval from 5 to 360°), and the related calculated quantities (wave number spectrum, wave frequency spectrum, significant wave height).

A. Altitude Determination

The exact flight altitude is determined by using the same radar returns as those used for the ocean wave analysis. At the small incidence angles used in the cases discussed here, and with the antenna lobe characteristics, the specular signal corresponding to the vertical backscatters enough energy in the antenna lobe to be detected in the spectrum: Fig. 2 shows the sharp rise associated with the vertical backscattered signal. The method to determine the altitude is to select the frequency bin (and thus the range bin) where the rise slope is the largest. In that case, the relative accuracy of the altitude determination is estimated to be within ± 1 bin position (i.e., ± 1.56 m).

B. Geometric Corrections

The position of the beam axis is known in the frame attached to the aircraft (Fig. 4): in this frame, which changes with the aircraft attitude (roll and pitch), the incidence angle of the beam axis θ_{bt} is 13.8°, and the rotation angle ψ varies clockwise from 0 to 360° at a constant rate of about one rotation per minute. However, in order to place the measurements in a geographic frame, it is necessary to determine the incidence angle of the beam axis θ_{bc} and the antenna rotation angle φ in a frame which does not change with aircraft attitude: this frame called here the "local reference frame" is defined by the vertical axis Z and by horizontal axes parallel and perpendicular to the aircraft heading (Fig. 4). The aircraft motions, and in particular roll, can induce modifications on the "true" incidence angle up to 2 or 3°. Once φ is determined it is easy to replace the measurements in the geographic frame (with respect to the North) by simply accounting for the aircraft heading angle. The azimuth angle calculated in this manner is identical to azimuth ϕ introduced in Section III.

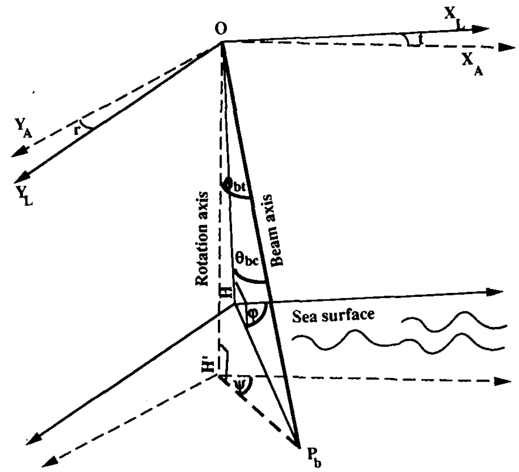

Fig. 4. Geometry of the measurement from RESSAC mounted on aircraft. The aircraft is supposed to be located at point "O", with a heading along the X_L axis. Geometry in two reference frames is shown: "local reference frame," L (solid lines), "aircraft reference frame," A (dashed lines). The transformation from frame A to frame L is expressed using the roll (r) and pitch (t) angles of the aircraft. See text for details (Section IV.B and Appendix C).

Each region sampled on the surface through the FM/CW principle corresponds to a frequency bin. The relation between the range R and the measured frequency f_m is given by

$$R = \frac{c}{2\mu} f_m + \frac{1}{\mu}[f_t V \cos(\phi - D) \sin\theta] \tag{13}$$

where the first right-hand term is relative to the frequency-distance relationship implied by the sawtooth frequency modulation of slope μ, and the second one is a small term accounting for the Doppler effect (Doppler frequency shift due to the relative speed projected on the look direction); c is the speed of light, f_m is the difference between the transmitted f_t and the received f_r frequencies at the same instant, V is the aircraft speed (along its route), D the drift angle due to the wind, and θ the incidence angle corresponding to the sampled point. Since θ and R are not independent ($\cos\theta = H/R$, where H is the flight altitude), an iterative procedure is used to determine both R and θ for each of the 400 sampled points.

C. Determination of the Modulation Function m

The fractional reflectivity modulation $m(x, \phi)$ due to the tilt of the long waves is given by (5), when expressed as a function of horizontal range x. Since the received power P_r is measured as a function of R and not x, it is first necessary to estimate the fractional reflectivity modulation $M(R, \phi)$ as a function of range R, for each azimuth angle ϕ. This is done by using the received power P_{r1} in the presence of tilt due to sea waves, and an estimate of the power P_{r0} that would be detected in the absence of long sea waves. In the case of a nontilted surface, and assuming that R and the normalized radar cross-section σ^0 (of a nontilted surface) are constant over the surface integration element, the radar equation can be written as:

$$P_{r0} = P_t G_{Mt} G_{Mr} \frac{\lambda_{em}^2}{(4\pi)^3} \frac{\delta R}{R^3} \sigma^\circ \int G_t G_r d\Omega \quad (14)$$

where $d\Omega$ is here the integration angle element in azimuth on the horizontal surface (with distance R kept constant), λ_{em} is the radar wavelength, P_t is the transmitted power, and the integral term accounts for the antenna gain pattern in transmission (subscript t) and reception (subscript r). The gains of the transmitting and receiving antennas at the beam center are G_{Mt} and G_{Mr}, respectively.

The fractional reflectivity modulation $M(R, \phi)$ is calculated as:

$$M(R, \phi) = \frac{W_1}{W_0} - 1 \quad (15)$$

where

$$W_{0,1} = R^3 P_{r0,r1} \left[\int\int G_t G_r d\Omega \right]^{-1} = R^3 P_{r0,r1} [I_G]^{-1} \quad (16)$$

It is obvious from (14) and (16) that the quantity W_0 used to calculate the modulation M through (15), is proportional to σ^0 of the nontilted surface. W_1 can be directly computed from (16) if the gain term I_G can be calculated. Since the gain function is known when expressed in the frame related to the antenna main axes (see Section III) it is necessary, in order to determine I_G, to calculate the coordinates of each point of the curvilinear integration path in the frame attached to the antenna. In order to reduce the consumption of CPU time required to compute I_G (which needs to be done for every radar return), I_G has been computed in advance for a large set of configurations of incidence, antenna rotation angle, pitch and roll, and then tabulated.

It has been assumed here that W_0 is a linear function of the range distance R, when expressed in dB. This was based upon three arguments: i) From previous studies (e.g., Valenzuela [24], Masuko *et al.* [26]) it appears that $|\sigma^0|_{\rm dB}$ (which differs from $\log(W_0)$ by a constant) is a gently decreasing function of θ in the incidence range 10–30°. ii) When processing our data by averaging the data over several circles to remove the tilt effects due to the sea waves, we found a linear decreasing function relating $\log(W_0)$ to θ. Fig. 5(a) shows one example of the mean variation of $\log(W_0)$ as a function of incidence angle θ. In this example the data have been averaged over five antenna rotations. It can be noted from Fig. 5(a) that after the gain integral I_G has been removed (through (16)) no significant short-scale feature from the antenna lobe pattern remains. iii) Although the dependence of $\log(W_0)$ versus range R (Fig. 5(b)) is not as close to a linear function as the one versus θ, we chose a first order (linear) approximation in order to decrease the cpu-time consumption in the adjustment process. Moreover, from Fig. 5(b) it appears that this linear approximation is quite reasonable, in the range of R corresponding to the 8–19° range in θ. Using this assumption, W_0 has been computed through a linear

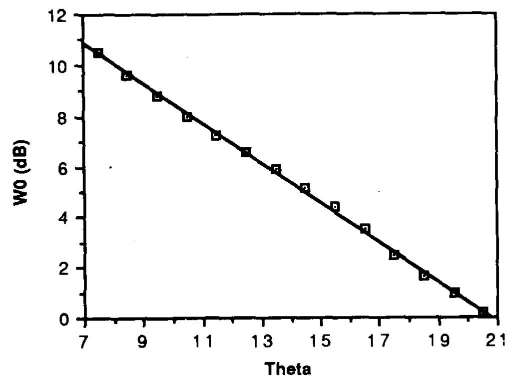

(a)

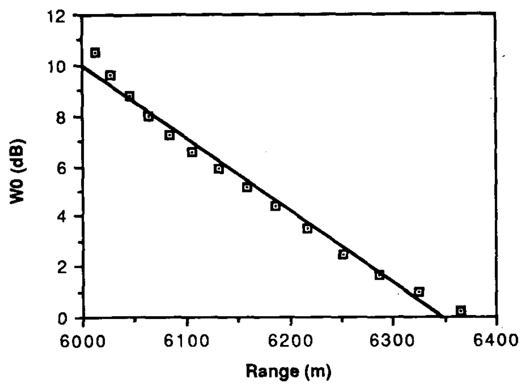

(b)

Fig. 5. Variation of the calculated power W_0 (received power corrected from distance and antenna gain functions, according to eq. (16), versus incidence angle (a), and range (b). These results were obtained by averaging RESSAC data over five complete antenna rotations (5 × 360°). In each case, the solid line shows the least-square fit.

adjustment process which minimizes:

$$\sum_R \{p(R)[\log(W_1(R, \phi)) - \log(W_0(R, \phi))]\}^2 \quad (17)$$

where $\log(W_0)$ is a linear function of $R(\log(W_0) = AR + B)$, and $p(R)$ is a weight chosen to counterbalance the more important weight given to the large incidence angles in the following processing step (projection on the horizontal axis).

The modulation $M(R, \phi)$, is then transformed into the modulation $m(x, \phi)$ expressed as a function of the horizontal distance x on the sea surface. A simple geometric projection is used to transform $M(R, \phi)$, into $m(x, \phi)$, with a constant horizontal sampling dx chosen as $dx = L_x/N_x$, where L_x is the elevation footprint (for incidence angles from 7 to 21°), and N_x the number of points which will be analyzed through the following Fourier transform. For the standard cases (6000 m altitude flight), and for the selected value of $N_x (N_x = 512)$, the horizontal sampling interval dx is 3.06 m. This projection leads to a better estimate of m for large incidence angles than for small ones, because at large incidences, several values of $M(R, \phi)$ will be averaged in the dx interval, while at low incidences, some values of m will be interpolated. This effect is compensated by the weight $p(R)$ chosen as $(1/\sin\theta)$ in the linear fitting described just above.

D. Determination of the Sea Surface Slope Variance v and of the Modulation Function m'

The modified reflectivity modulation $m'(x,\phi)$ is related to the reflectivity modulation $m(x,\phi)$ through (12). It is clear from (12) that one needs to know the slope variance v in order to determine $m'(x,\phi)$, whereby the sea surface slope spectrum $K^2F(K,\phi)$ is obtained through (7) and (8). Rather than using external wind measurements from buoys, we compute the parameter v from the radar data themselves, by analyzing the dependence of the observed radar cross-section with incidence angle. Combining (1) and (10), one gets:

$$|\sigma^0\cos^4\theta|_{\mathrm{dB}} = 10\log_{10}\left(\frac{\rho}{2\sigma_u\sigma_c}\right) - \frac{10\log_{10}e}{v}\tan^2\theta. \quad (18)$$

Obviously, a linear fit to the experimental values $|\sigma^0\cos^4\theta|_{\mathrm{dB}}$ expressed as a function of $\tan^2\theta$ would yield two parameters (ordinate at the origin and slope of the linear function) both related to the slope variance v. Evaluating v from the ordinate at the origin would require the parameter ρ (i.e., the diffraction-modified Fresnel reflectivity as introduced in (1)) to be known precisely. Furthermore, it would require a precise absolute calibration of σ^0. On the contrary, the determination of the slope of the linear function fitted to $|\sigma^0\cos^4\theta|_{\mathrm{dB}}$ versus $\tan^2\theta$, yields the slope variance v directly without further assumptions. Therefore, we have chosen to use this latter method to determine v, with $|\sigma^0|_{\mathrm{dB}}$ replaced by the quantity $10\log(W_1)$ which differs by a constant from $|\sigma^0|_{\mathrm{dB}}$ and whose estimate does not require an exact calibration of the radar.

E. Determination of the Modulation Spectrum

To calculate the modulation spectrum $P'_m(K,\phi)$ (see (7)), a real 512 point FFT is applied to $[m'(x,\phi)H(X)]$, where $H(X)$ is the Hanning window. The use of the Hanning window allows to reduce the side lobe effects in the spectral domain at the expense of a slight broadening of the spectral peaks (1.44 bin in the spectral domain). Moreover, the multiplication by the Hanning window gives more weight to the values of m' around the center of the sample, which corresponds roughly to the incidence of the beam-axis, and hence to the best estimated values of m'. The real FFT provides spectral energy in 256 wave number intervals, with a wave number increment $dK = 2\pi/L_x$. This corresponds to wavelengths Λ from about 6 to 1566 m. However, it is unreasonable to give a physical meaning to spectral components corresponding to $\Lambda > 400$ m nor to $\Lambda < 30$m (see Section III). Therefore, only the 64 first wave numbers are considered ($\Lambda > 25$m), and the three lowest wave numbers (which correspond to $\Lambda > 520$m) are ignored. The wave number resolution is 1.44 times $dK(5.78\times10^{-3}$ cpm for 6000 m altitude flights). This yields a wavelength resolution $\Delta\Lambda = 1.44\Lambda^2/L_x$: a 100-m wavelength is determined with a ±9m accuracy for a 6000 m flight level.

F. Corrections Applied to Obtain the Sea-Surface Height Spectrum

The computed modulation spectrum $P'_m(K,\phi)$ then needs to be corrected in order to account for (i) speckle noise and radar response function, and (ii) footprint displacement within the integration time.

1) Correction from Speckle Noise and Radar Response Function: Introducing the effects of the speckle and the pulse waveform, Jackson *et al.* [21] have shown that the modulation spectrum of the backscattered power $\delta P_r/\langle P_r\rangle$ of the signal effectively received by the radar can be expressed as:

$$P(K,\phi) \approx S_R(K)P_m(K,\phi) + (1+\eta^2(\phi))S_N(K) \quad (19)$$

where: $\eta(\phi) = \langle m^2(x,\phi)\rangle^{1/2}$ is the rms modulation depth (whose square $\eta^2(\phi)$ is of a few percent, and will be further neglected as compared to 1). The other quantities introduced in (19) are the spectrum of the response function $S_R(K)$, and the power fading (or speckle) spectrum $S_N(K)$:

$$S_R(K) = \exp\left(-\frac{K^2}{2K_p^2}\right) \quad (20)$$

$$S_N(K) = \frac{1}{N\sqrt{2\pi}K_p}\exp\left(-\frac{K^2}{2K_p^2}\right) \quad (21)$$

$$K_p = \frac{2\sqrt{\ln 2}}{\Delta x} \quad (22)$$

in which Δx is the horizontal resolution, expressed as the half-power width of the resolution cell, assumed to be of Gaussian shape. N is the number of independent samples. $P_m(K,\phi)$ is the modulation spectrum (defined in the same way as $P'_m(K,\phi)$ in (7), except that $\langle m'(x,\phi)m'(x+\xi,\phi)\rangle$ is replaced by $\langle m(x,\phi)m(x+\xi,\phi)\rangle$).

Equation (18a) of Jackson *et al.* [21] contains an additional dc term $\delta(K)$ which does not appear here because the modulation spectrum (i.e., the spectrum of $\delta P_r/\langle P_r\rangle = (P_r - \langle P_r\rangle)/\langle P_r\rangle)$ is taken here, instead of the spectrum of $P_r/\langle P_r\rangle$.

It is to be noted that the horizontal resolution Δx quoted here takes into account all sources of smearing which occur before detection. These include the FFT procedure in the real-time analyzer, as well as smearing related to phase fluctuations of the FM signal (hereafter called phase noise). The speckle noise $S_N(K)$ and the spectrum of the radar response function $S_R(K)$ are both fully determined if K_p (or, equivalently, Δx) and N are known. Those two quantities have been experimentally estimated (see Appendix). The results give strong support to the relevance of Jackson's approach, and to the assumption that the samples are independent. For our experimental setup, we found $K_p = 0.112$ rad/m (i.e., $\Delta x =$ 14.9m), and $N = 32$.

Fig. 6(a) illustrates the effect of speckle correction, where one ignores for the moment the radar response function correction (therefore, taking $S_R(K) = 1$ in (19)). It is found that the energy density spectrum has an amplitude significantly larger than that of the speckle noise for all the 64 first wavenumbers, i.e., for wavelengths larger that 25 m. When applying the speckle noise correction, the mean significant wave height, which is related to the energy of the spectrum (see below, (25)–(26)), is decreased by 20%. This shows that speckle noise

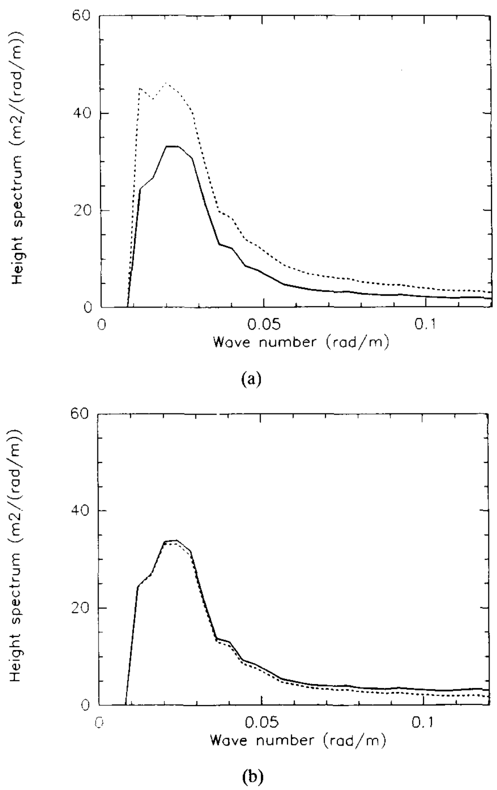

Fig. 6. (a) Example of a sea-wave nondirectional spectrum, obtained from the RESSAC data before and after applying the correction due to speckle noise (shown respectively by the dashed and solid lines). (b) Same as in (a), but for results obtained before and after applying the correction due to the radar response function; the solid line shows the same spectrum as the corrected one in (a), the dashed line shows the spectrum after correction due to the response function. In (a), (b), the horizontal axis covers a range in wave number limited to the 30 first wavenumbers retrieved from the data processing.

correction is essential if one wishes to estimate the physical quantities associated to the wave spectra.

The effect of the radar response correction (performed according to (19)) is illustrated in Fig. 6(b). The correction is very small for wavelengths larger than 80 m. Overall, there would be a 4% underestimate of the mean significant wave height, if this correction were not taken into account.

2) Footprint Displacement: The second perturbating effect on the received radar signal is related to the footprint displacement due to rotation of the antennas, and to the aircraft motion during the integration time (usually 0.208 s).

The antenna rotation angle is 1.2° for a 0.208-s integration time. Correlatively the footprint moves laterally. However this displacement represents only a small change of the azimuth footprint: 4% at the center of the footprint for a 6000-m flight level. Therefore, this effect has been neglected in the processing.

The footprint displacement due to the aircraft speed is much more important, particularly when the plane of incidence is aligned along the aircraft route. This effect is taken into account by writing that the modulation $m'(x, \phi)$ is convolved by a rectangular window of width L_A:

$$L_A = VT_{\text{int}} \cos(\varphi - D) \tag{23}$$

where T_{int} is the integration time, and D the aircraft drift angle due to the wind.

To correct the results of this effect, the wave modulation spectrum is divided by the spectrum $S_A(K)$ of the rectangular window:

$$S_A(K) = \frac{\sin^2(L_A \cdot K/2)}{L_A \cdot K/2}. \tag{24}$$

The correction due to footprint displacement is of the same order of magnitude as the response function correction, for typical aircraft speeds of 100 m $\cdot$ s^{-1} and when the incidence plane is parallel to the aircraft route. However, when integrated over all the directions, the effect of neglecting this correction would produce only a 2% underestimate of the mean wave height.

G. Computing and Averaging the Sea Wave Spectrum

Once corrected according to the procedure indicated above, the modulation spectrum P'_m is transformed into a sea wave slope spectrum $K^2(F(K, \phi)$ through (8). The result consists of wave slope spectra as a function of K and ϕ for each rotation ($\approx 1\text{min}$). In order to reduce the statistical fluctuations inherent in the sea surface phenomena, averaging procedures are applied: smoothing averages are performed both in the azimuth direction ϕ and along the aircraft surface track. In the azimuth direction, a 15° smoothing average is applied and the slope spectra are resampled each 5°. Along the track, data are usually averaged with a smoothing procedure over five complete antenna rotations. For five consecutive rotations, this corresponds to a 30-km horizontal scale, for an aircraft speed of $100\text{m} \cdot \text{s}^{-1}$.

H. Determination of Useful Physical Quantities

The wave slope spectrum is converted into a wave height spectrum $F(K, \phi)$ through a mere division by K^2, where $K(= 2\pi/\Lambda)$ is expressed in rad/m and F in $\text{m}^2/(\text{rad/m})^2$.

When integrated over all the directions, the nondirectional height spectrum is $F_{\text{HND}}(K)$:

$$F_{\text{HND}}(K) = \int_0^{2\phi} F(K, \pi) K d\phi. \tag{25}$$

The significant wave height is computed as four times the square root of the height variance, namely:

$$H_s = 4\sqrt{\int_K F_{\text{HND}}(K)\, dK} \tag{26}$$

with K limited for this calculation to the 30 first wave numbers, which corresponds in the conditions of the experiments described hereafter to wavelengths larger than 52 m.

For intercomparisons between buoy and radar measurements, the nondirectional frequency spectrum $F_f(f)$ has also been calculated, using the dispersion relation of waves over large water depths:

$$F_f(f)df = F_{\mathrm{HND}}(K)dK \tag{27}$$

with

$$df = \frac{dK}{4\pi}\sqrt{\frac{g}{K}}.$$

V. Experiments and Results

A. Experiments and Data Sets

Since the RESSAC system became operational, it has been used in three different experiments. Among these, data from the first two experiments have been used for the present paper. The first one, called "RENE" ("Rehearsal experiment ERS1-validation, Northern Europe")[1] was defined and organized by the European Space Agency (ESA) as a rehearsal campaign preparing for the ERS1 Calibration/Validation (CAL/VAL) experiment, which is planned for the end of 1991, after the launch of ERS1. The second experiment in which RESSAC was involved was mainly a technical experiment, whose aim was to test the RESSAC system when mounted on board the French Meteorological aircraft "Merlin-IV". It took place in May 1990, off the Atlantic coast of Brittany in France. Most of the flights performed with RESSAC during this experiment were defined to test the effective characteristics of RESSAC: data have been recorded in order to estimate the speckle noise level and the radar response function (see Section IV and Appendix), and to check the antenna pattern in elevation (Fig. 3) from flights over corner reflectors. The third experiment took place recently (February 1991) and will be the subject of future publications.

The main goal of RENE was to verify the performance of the various instrumental means (buoy network, instrumented ships, and aircraft) which will be used in 1991. RENE took place over the Haltenbanken area, off the coasts of Norway in February–March 1990. During this experiment RESSAC was mounted on board the DORNIER 228 of the German

DLR, flying at about 20 000 feet ($\approx$6000 m) at a speed of 80 to 120 ms^{-1}. We present here results obtained from the measurements performed on February 19, 1990.

From the RESSAC data, ten mean directional spectra, averaged over five complete antenna rotations have been deduced. These results cover a time period of about 1 hour (from 12:58 to 13:55 UT). Fig. 7 indicates their respective geographic locations along the flight. In order to validate the results obtained from RESSAC, we have used other available sources providing information about sea-state or wind: wind and wave buoy measurements, ship-mounted radar observations, and wave model hindcasts. The buoy measurements were performed by two instrumented buoys called TOBIS 7 and TOBIS 10 (or T7 and T10, respectively), deployed by the Norwegian company OCEANOR, and moored over 250 and 1260 m water depth, respectively. They provided 20-min averaged values of wind direction and wind speed, and nondirectional frequency spectra of the sea elevation, from measurements integrated over 35 min of acquisition [27]. The ship-radar used in this study is the one deployed by GKSS on the German research vessel "GAUSS". It provided two-dimensional images of the surface from grazing incidence observations, from which directional spectra have been deduced. Also deployed from the vessel, was a waverider buoy (Datawell) providing frequency spectra integrated over a 30-minute time interval. In addition, hindcasts of the Norwegian wave model "WINCH" have been used for comparisons. This latter is a so-called "second-generation," spectral wave model, which has a 70 km horizontal resolution, and uses input wind fields taken from the Norwegian limited area weather-forecast model. A directional buoy was supposed also to be moored, but due to the very bad sea conditions, this was unfortunately not possible. Fig. 7 shows the position of the mean wave spectra retrieved from RESSAC, together with the position of the TOBIS buoys, the Gauss vessel, and the nearest WINCH model grid points.

[1]The name RENE was chosen to honor the memory of René Bernard who initiated this study and died prematurely in February 1990.

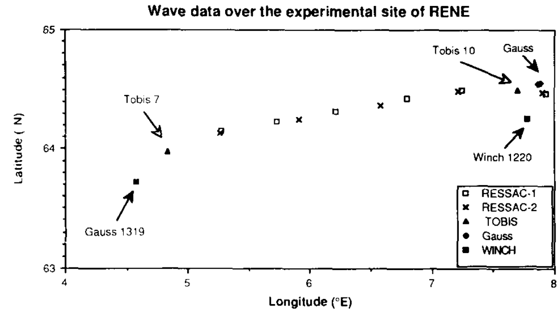

Fig. 7. Geographic position of the mean wave spectra obtained from the processing of the RESSAC data, plotted as a function of their longitude and latitude: white squares for the mean spectra obtained from the flight from T10 to T7 (from 12:58 to 13:41 UT), and crosses for those obtained from the flight back from T7 to T10 (from 13:41 to 13:55 UT). The position of the other wave data is also shown: black triangles for the TOBIS 10 (T10) and TOBIS 7 (T7) buoys, black squares for the two closest grid points of the WINCH model (numbered 1220 and 1319), and black diamond for the research vessel GAUSS, operating the GKSS radar and the waverider buoy. Two different symbols are used for the RESSAC data.

The meteorological situation, as known from the synoptic surface charts of February 19 and 20 indicates that a general and persistent South-West surface flow was associated with a low pressure center. This latter moved from (55°N, 21W) to (62°N, 12W) between 00:00 and 12:00 UT on the 19th of February. Moreover, the surface charts at 12:00 UT indicate that a secondary frontal discontinuity associated with this low pressure center approached the Haltenbanken area, and provoked a wind shift from SW to SE. Hence, at the time of the RESSAC measurements, the wind was temporarily blowing from SE, although the general and persistent surface flow was from SW. In fact, at 18:00 UT the wind direction over the Haltenbanken area was again from SW.

B. Mean Slope Variance

Fig. (8) displays one example of the variation of the inferred slope variance v as a function of time. As the antenna rotates, different azimuth directions are explored versus time. As observed in Fig. (8), v exhibits a periodic variation, with two

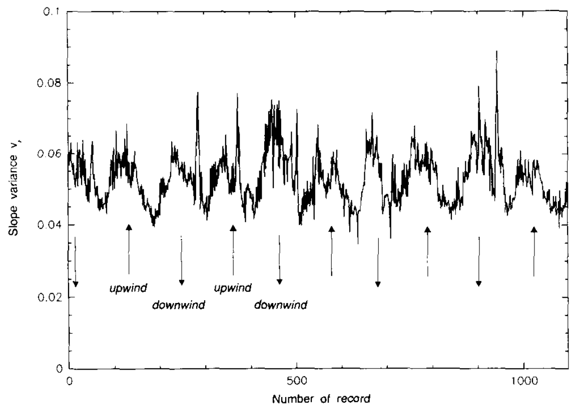

Fig. 8. Time variation of the sea surface slope variance v, as defined by (15), and inferred from the RESSAC measurements in the vicinity of buoy T10. The whole time interval displayed covers a period of about 5 min, over which the antenna performed a little less than five rotations. The times at which the radar is looking upwind, and downwind (as deduced from the T10 buoy measurements) are indicated by arrows.

maxima and two minima over a 360° azimuth range. The TOBIS buoy measurements (Fig. 9(a)) indicate that the two maxima correspond to the upwind and downwind directions, and the two minima to the crosswind directions. This is remarkable since it opens the way to the determination of the wind speed direction (modulo a 180° ambiguity) from the examination of the variations of the parameter v with azimuth angle. One can compare these results with the clean sea model of Cox and Munk [28], which was constructed from optical measurements, and gives the upwind and crosswind slope variances (σ_u^2 and σ_c^2) as a function of the wind speed U:

$$\sigma_c^2 = 0.003 + 1.92 \times 10^{-3} U$$
$$\sigma_u^2 = 3.16 \times 10^{-3} U.$$

For a given radar look direction in azimuth, v is related to σ_u^2 and σ_c^2 through (11) which gives in particular $v = 2\sigma_c^2$ in the crosswind direction, and $v = 2\sigma_u^2$ in the upwind direction. Fig. 9 indicates that a wind speed value of about 11 m/s is observed at the time and in the region of our radar measurements. The model of Cox and Munk with a wind speed of 11 m/s yields $2\sigma_c^2 = 0.0482$ and $2\sigma_u^2 = 0.0696$, and $\sigma_c^2/\sigma_u^2 = 0.69$. Our radar-inferred values (Fig. 8) of v are somewhat smaller than these model values, and oscillate between ≈ 0.04 (crosswind value) and ≈ 0.06 (upwind value), with a comparable anistropy ($\sigma_c^2/\sigma_u^2 \approx 0.66$). Because our data have been obtained at C-band (wavelength = 5.6 cm), the backscatter radar signal is not sensitive to the spectral components of the sea waves which are below $\approx$ 20 cm, which corresponds to the diffraction limit. This can explain that our radar inferred values of slope variance v tend to be smaller than those inferred from optical measurements. Also, Cox and Munk's model is based upon a limited number of observations, and one cannot expect then the present situation to fit the model perfectly. Therefore, rather than using the Cox and Munk's model, we have chosen to use here the radar inferred values of v, since they are relevant for the purpose

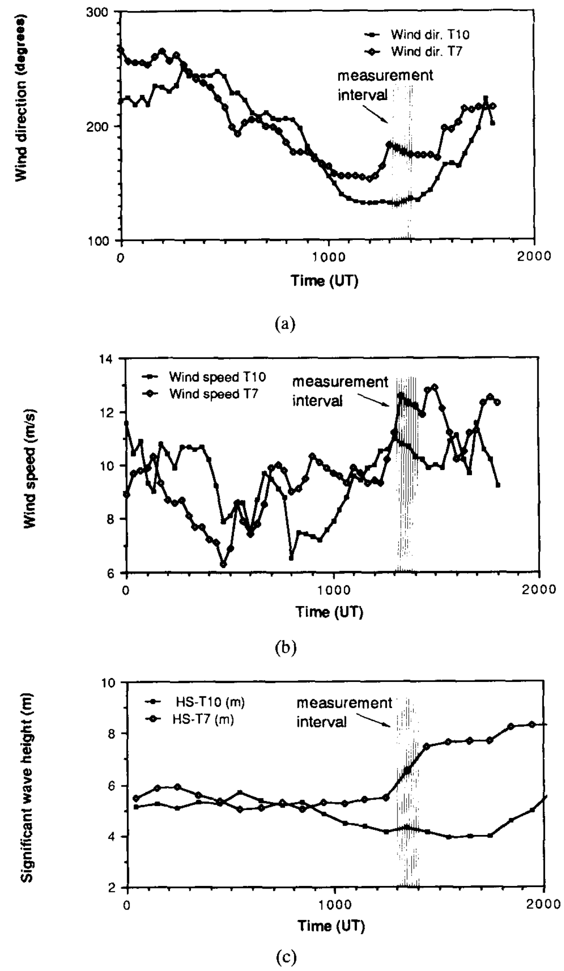

Fig. 9. Time series of the TOBIS buoy measurements on February 19, 1990: (a) wind direction, (b) wind speed, (c) significant wave height. In each case, the solid squares refer to T10, and the open lozenges to T7. The hatched areas correspond to the RESSAC measurement interval.

of relating the radar-inferred modulation spectrum to the sea wave spectrum (7), (8), (12).

It is to be noted that the interpretation of v (as determined through (18)) in terms of the slope variance, rests on the assumption that the backscatter is dominated by quasi-specular reflection (1). In order to assess this assumption, one can use the model of Brown [25], who estimated the contributions to σ^0 from both quasi-specular and Bragg returns, as function of wind speed, radar frequency, and polarization. For the present case (wind speed$\approx$11 m/s, 5.35 GHz, HH polarization), we found that, whereas the quasi-specular return dominates at low incidence angles, both contributions become equal for an incidence angle $\theta \approx 21°$. Since our range of explored incidence angles is from 7° to 21°, it is entirely dominated by specular reflection in this case. For lower wind speeds however, the situation is much less satisfactory. For example, at 4 m/s wind speed, both contributions are equal for $\theta \approx 16°$, which is well inside our range of incidence angles. Indeed, the average profiles of $(\sigma^0 \cos^4 \theta)$ that we observed do not

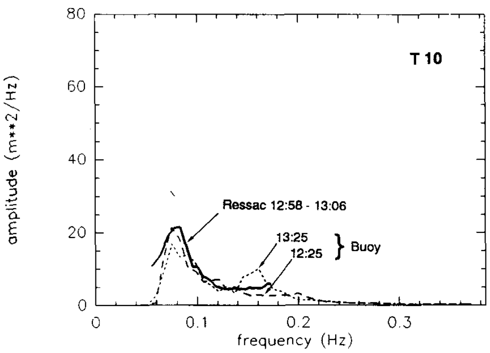

(a)

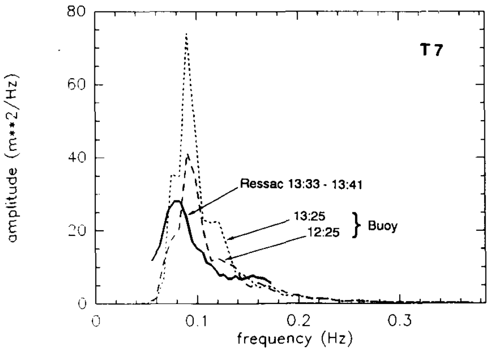

(b)

Fig. 10. Comparison of nondirectional spectra obtained from RESSAC (solid curve), and from the TOBIS buoy measurements (short and long dashed curves). (a) Mean RESSAC spectrum in the vicinity of T10 obtained from the data recorded between 12:58 and 13:06 UT, with the T10 spectrum at 12:25 UT (long dashed) and 13:25 UT (short dashed) superimposed; the RESSAC spectrum is plotted in the frequency range corresponding to the 30 first wavenumbers retrieved from the processing. (b) Same as (a), but for the RESSAC spectrum near T7, obtained from the data recorded between 13:33 and 13:41 UT, with the T7 spectra at 12:25 and 13:25 UT superimposed.

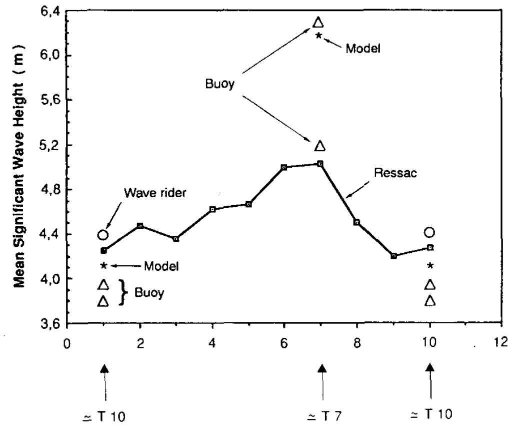

Fig. 11. Mean significant wave height calculated from the RESSAC data (solid line), for each of the ten mean spectra along the T10–T7 and T7–T10 tracks (see the positions in Fig. 9). Also shown is the mean significant wave height given by the T10 and T7 buoys at 12:25 and 13:25 UT (triangles), by the WINCH model (stars), and by the waverider buoy (circles).

usually follow closely the Gaussian profile (as function of $\tan\theta$) which would be expected from (18). To account for it, in more recent versions of our algorithm, we replaced (18) by an empirical second order polynomial fit. This modified version should in principle have a more general applicability. However, the empirical parameters then retrieved from the polynomial fit, in contrast to the slope variance v, do not have any more a simple physical meaning.

C. Wave Spectra

1) Nondirectional Spectra: The nondirectional spectra derived from the RESSAC data have been calculated according to (25), (27) (assuming the dispersion relation of waves over large water depths). They have been compared to the frequency spectra given by the TOBIS buoys. Fig. 10 shows a comparison of RESSAC spectra obtained near T10 (observation beginning at 12:58 UT) and T7 (observation beginning at 13:33 UT), to TOBIS spectra at two successive sampling times (sampling beginning at 12:25 and 13:35 UT). It is seen that for the T10 observations (Fig. 10(a)), the agreement is excellent over the frequency range corresponding to the RESSAC's 30 first wavenumbers (0.055–0.173 Hz). The significant wave height, computed from RESSAC over this frequency range (4.25 m) differs only by 6 to 11% from the T10 results (3.84 m at 12:25 UT, 4.01 m at 13:25 UT). For the T7 observations (Fig. 10(b)), the agreement is less satisfactorily, although the significant wave heights from RESSAC (5.03 m) and from T7 (5.21 m at 12:25, 6.33 m at 13:25) differ only by 3% at 12:25 UT (20% at 13:25 UT). The spectral peak observed from the T7 data is larger and narrower than that seen by RESSAC. It seems that the discrepancies in that case can be attributed to sea-state variability in time and space (the two sets of measurements are not exactly coincident) due to the approach of the above-mentioned low pressure center: a rapid increase of the significant wave height is observed (Fig. 9(c)) beginning at 12:00 UT at T7, but later (at 17:00 UT) at T10.

Although the agreement between RESSAC and TOBIS7 is not excellent, it must be noted that the results from RESSAC indicate, as expected from the TOBIS buoys, significant wave heights larger over T7 than over T10. This is also seen in Fig. 11, which shows the RESSAC-inferred significant wave heights plotted as a function of the observation number (1–10), with values from TOBIS buoys, WINCH model and waverider buoy plotted at the abscissa point corresponding to the closest (in time and space) RESSAC observation. From Fig. 11 it appears that over the T10 area, the significant wave height derived from RESSAC has the same order of magnitude as the one deduced from all the sources of data, while over the T7 area, there are large differences from one source of data to the other, although all of them, including RESSAC indicate much larger values over T7 than over T10.

2) Directional Spectra: Two examples of directional spectra, corresponding to the two spectra shown in Fig. 10, are presented in Fig. 12, as polar plots. In these figures the contours are shown over the 0–360° azimuth range; no attempt has been made to remove the ±180° ambiguity from the RESSAC data alone. It appears that the RESSAC spectra are not completely symmetrical, although the differences at

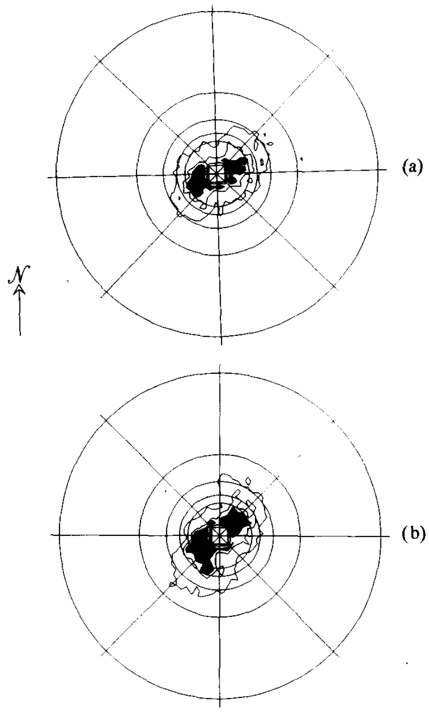

Fig. 12. Mean directional spectra obtained from the RESSAC data, (a) in the vicinity of T10 between 12:58 and 13:06 UT, (b) in the vicinity of T7, between 13:33 and 13:41 UT. The figures are shown as polar plots, with the direction given by the angle from North (North indicated by an arrow), and the wavelength given by the distance from the center; the scale in wavelength is given by the five circles plotted every 50 m, from 50 m (outer circle) to 250 m (inner circle). The isolines are plotted for the levels 100, 500, and 1000 $m^2/(rad/m)^2$, with levels greater than 1000 $m^2/(rad/m)^2$ in black.

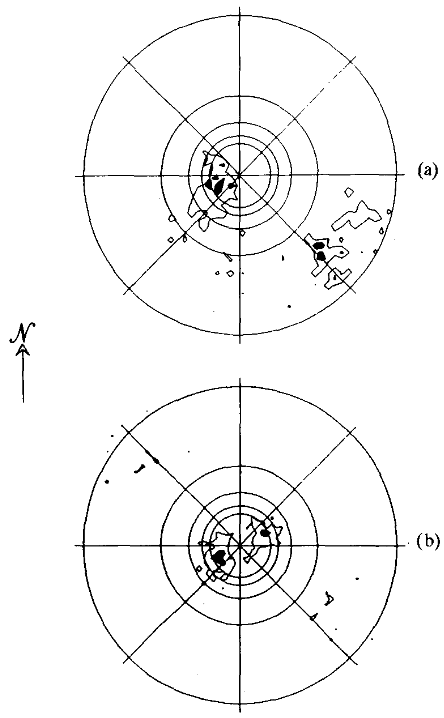

Fig. 13. (a) Image spectrum obtained from the GKSS radar measurements on ship GAUSS at 14:06 UT, and (b) RESSAC mean directional slope spectrum between 13:55 and 14:01 UT near T10. Same representation as in Fig. 12, except that the isolines in (a) give the spectral levels in relative amplitudes (relative levels: 1 to 3, with values greater than those of level 3 in black), while in (a) they are for the levels 0.15, 0.5, 0.8 m^2.

$\pm 180°$ are not high. From this single set of data, it was not possible to determine whether this effect was due to statistical errors, or to some geophysical processes. This question will be addressed in the future by analyzing results of other situations. The spectra of Fig. 12 exhibit a main peak corresponding to a swell system with a 313 m wavelength and propagating along the SW–NE direction. The synoptic meteorological charts, and other sources of data (see below) indicate that the propagation direction is in fact from SW. Note that in this particular case, the dominant waves do not propagate along the wind direction observed at the same time (≈ 130 to $150°$). In fact, this SW swell is associated with the large-scale persistent surface flow, although the wind was temporarily from SE in front of the secondary discontinuity approaching the experimental site. As found on the non-directional spectra, the directional spectra of Fig. 12 show a significant difference between the surface signatures near T10 and near T7: the angular distributions are different, with an anticlockwise shift of about 25° of the wave components at T7 (as compared to the ones at T10). This also corresponds to a difference in the wind direction measured 10 hours prior to the radar observations (Fig. 9(a)).

The directional spectra from RESSAC have been compared to results provided by the GKSS from the ship-radar observations. Fig. 13 shows an example of directional spectra obtained near 14:00 UT in the vicinity of T10 with the GKSS radar (Fig. 13(a)) and with RESSAC (Fig. 13(b)). In the GKSS display, the $\pm 180°$ ambiguity has been removed, and the contour levels indicate only relative amplitudes, because the data have been processed without taking into account the radar transfer function, thus giving a mere image spectrum. Fig. 13(a) may thus be closer to the slope spectrum $K^2F(K, \phi)$. In order to allow a more relevant comparison, the RESSAC spectrum displayed in Fig. 13(b) is therefore taken as the directional slope spectrum $K^2F(K, \phi)$, in contrast to Fig. 12 where height spectra $F(K, \phi)$ were displayed. In Fig. 13, the GKSS spectrum and the RESSAC spectrum together indicate that the dominant waves have a 250 m to 350 m wavelength and propagate from SW ($\approx 240°$). A second wave system propagating almost along the wind direction ($\approx 130°$) and with short wavelengths ($\approx 75\mathrm{m}$) appears very clearly on the GKSS spectrum displayed. These wind-sea waves are also detected by RESSAC, with approximately the same direction and wavelength, although with less relative intensity. It is to be noted, however, that this secondary system exhibits a somewhat sporadic behavior in the GKSS data, and some other spectra were obtained by GKSS a few tens of minutes before, which did not show these wind-sea waves at all. Quantitative comparison of absolute levels between both instruments is therefore uneasy (and has not been attempted), but the comparison between both instruments turns out to be excellent in terms of wavelength and direction, for the swell as well as wind-sea wave components.

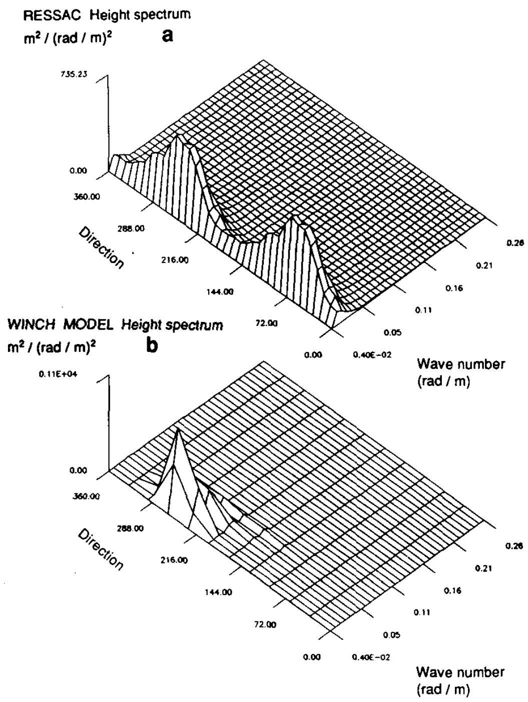

Fig. 14. Comparison of directional spectra obtained from (a) RESSAC, between 12:58 and 13:06 UT in the vicinity of T10, and from (b) the WINCH model (at grid point 1220, at 12:00 UT). The spectra are plotted in 3-D, with one horizontal axis labeled by wave numbers in rad/m (64 wave numbers), and the second horizontal axis labeled by the direction from North.

Comparisons have also been performed between RESSAC results and the WINCH model outputs. Fig. 14 shows the directional spectra in 3-D plots (spectral energy density versus direction and wave number), from RESSAC at 12:58 UT (Fig. 14(a)), and from the WINCH model output (Fig. 14(b)) at 12:00 UT, at grid point 1120 (i.e., 30 km away from the RESSAC observations at 12:58 UT, see Fig. 7). The WINCH directional spectrum is shown without the $\pm 180°$ ambiguity. Although the RESSAC directional spectrum tends to be broader in azimuth than the WINCH model, the maxima of the height-spectra occur at nearly the same azimuth (250° for RESSAC, 240° for WINCH).

In summary, the directional ocean wave spectra retrieved from RESSAC are consistent with the information provided by the other sources of data. Unfortunately, no directional buoy measurement was available to provide an additional means of validation.

VI. Conclusion

We have presented the French radar system called RESSAC, used from aircraft platforms for measuring directional spectra of ocean waves in the gravity domain (wavelengths from 30 to 400 m). The advantage of this radar, which is a *C*-band, FM/CW (Frequency Modulated/Continuous Wave) system, lies in its small cost, low power, and high range resolution. It has been designed to be used from aircraft flights at about 6000 m. The transmitting and receiving antennas are looking at near-vertical incidence ($\approx 14°$ incidence) and rotate around a vertical axis.

The data processing used to retrieve directional spectra is based upon the linear model proposed by Jackson *et al.* [21, 22], which allows one to relate in a simple way the modulation of the backscattered e.m. energy along the look direction to the slope of the waves in the gravity domain. With respect to the work of Jackson *et al.*, the calculation of the tilt modulation transfer function has been slightly improved: i) The known antenna gain-pattern is removed from the recorded signal; this is done by taking into account the attitude of the platform to calculate the position of each sampled point located within the beam-spot at the surface. ii) The tilt modulation transfer function is used without the assumption of a constant incidence angle. iii) The variance of the slope probability density function (assumed of Gaussian shape) is estimated from the radar data alone and introduced in the tilt modulation transfer function.

The first results obtained from RESSAC are presented in this paper and compared to other data sets: nondirectional frequency spectra from buoy measurements, directional spectra from a ship-radar and from a sea-state model. The consistency is in general very satisfactory: near one of the two buoys which serve as reference, the agreement between the various data sets is very good (in direction, peak period, and significant wave-height), whereas near the other buoy, the differences may probably be explained by temporal and/or spatial variations of the sea-state. The method developed to estimate the slope probability density function gives results consistent with the wind observations and with previous results found in the literature. This tends to indicate that RESSAC observations can be used to get at the same time, information about sea-waves in the gravity domain, and about the wind (at least about the wind direction).

One has to note however, that this study concerns only one situation, in which the dominant waves did not propagate along the wind direction. A full assessment of the quality of the data and of the processing, will only be reached after performing the same analysis over various sea-state situations. Unfortunately, some technical problems due to the youth of the RESSAC system, prevented us from analyzing more than one situation. New data sets have been recently collected during SWADE (Surface Wave Dynamics Experiment near Wallops Island off the US East-coast, organized by ONR and NASA), and RESSAC was involved in the ERS-1 geophysical validation campaign in Norway (end of 1991). The SWADE data analysis will notably give the opportunity to compare results obtained from RESSAC, from the ROWS developed by Jackson *et al.* and from the surface contour radar [18], [19].

Acknowledgment

The RESSAC system has been developed under the support of the European and French space agencies ESA and CNES. We thank the Norwegian company OCEANOR, and particularly Tom-Ivar Bern for providing computational support during the RENE campaign, and the buoy reference data after the campaign. We are very grateful to Friedwart Ziemer from GKSS (Germany) who provided us with the ship-radar data, and Johannes Guddal from the Norwegian meteorological office (DNMI) for providing the WINCH model outputs. Thanks also to David Offiler from the UK meteorological office for providing useful information about the meteorological situation. Also we thank the members of the German institute DLR who operated the Dornier 228 aircraft during the RENE campaign, and the members of the French meteorological office METEO-FRANCE", who operated the Merlin-IV aircraft during the Brittany experiment.

VIII. Appendix
Semi-Empirical Estimation of the Speckle Noise and the Radar Response Function

During the campaign held in Brittany in May 1990, some flights were performed over the sea, in which a number of 8 samples (instead of 32) were integrated before recording on tape. Four series of 48 consecutive spectra were thus selected as indicated below. These were processed in two different ways:

1) In the first processing, the modulation spectrum was computed from each recorded radar spectrum. The 48 modulation spectra were then averaged, leading to the spectrum $P_8(K)$ (where the subscript 8 refers to the number of independent samples averaged before computing the modulation spectrum).
2) In the second treatment, the recorded radar spectra were first post-integrated n times ($n = 2$ or 4). The modulation spectra were then computed from every post-integrated spectrum, and then averaged, leading to the spectrum $P_{8n}(K)$.

Hence, $P_8(K)$ contains the signal, together with the speckle noise relevant to eight integrations, $S_8(K)$. From (19) (with $\eta^2(\phi)$ neglected as compared to 1, one gets:

$$P_8(K) = S_R(K)P_m(K,\phi) + S_8(K). \tag{A1}$$

Similarly:

$$P_{8n}(K) = S_R(K)P_m(K,\phi) + S_{8n}(K). \tag{A2}$$

Hence, by substraction:

$$P_8(K) - P_{8n}(K) = S_8(K) - S_{8n}(K). \tag{A3}$$

We make here the assumption that the 8-time integrated samples are independent. The relevance of this assumption will be checked *a posteriori.* Within this assumption, further integration of n samples should reduce the noise variance by a factor n. Therefore:

$$S_{8n}(K) = \frac{1}{n}S_8(K). \tag{A4}$$

Combining this equation with the same equation applied to the specific case $n = 4$ yields:

$$S_{32}(K) = \frac{n}{4}S_{8n}(K). \tag{A5}$$

Combining (A3), (A4), and (A5), we get:

$$S_{32}(K) = \frac{n}{4}\frac{(P_8(K) - P_{8n}(K))}{(n-1)}. \tag{A6}$$

This procedure is valid only if we can assume that the sea-wave modulation signal builds up coherently when post-integrations are performed, so that $P_m(K,\phi)$ actually vanishes when equations (A1) and (A2) are subtracted. This requires the antenna beam spot not to move along the x direction during the integration time. In order to be in the optimal situation, we selected the spectra obtained when the antenna was looking in the direction perpendicular to the airplane route (i.e., the antenna rotation angle φ and the airplane drift D satisfy: $\varphi - D = 90°$). Furthermore, in this configuration, the displacement of the beam spot along the y direction due to the antenna rotation and due to the aircraft velocity partially counterbalance each other, and it was therefore preferred to the opposite configuration ($\varphi - D = 270°$).

The function $S_{32}(K)$ has been computed from the data through (A6). We found that $S_{32}(K)$ can be well approximated by a Gaussian function over the range $K \leq 0.4$ rad/m. The part of the spectrum which is relevant to the determination of the ocean wave spectra is limited to $K \leq 0.2$ rad/m (i.e., $\Lambda \geq 30$ m) since, outside this range, limitations of the measurement technique occur as indicated in section III. Therefore, we have least-square fitted the two parameters N and K_p of the Gaussian function (20) to the experimental values $S_{32}(K)$ within the domain $K \leq 0.2$ rad/m. We rewrite (20) as

$$S_{32}(K) = \frac{1}{N\sqrt{2\pi}K_p}\exp\left(-\frac{K^2}{2K_p^2}\right).$$

Over the four series of 48 radar spectra processed with $n = 2$, we obtained an average value of 33.7 for N and 0.1127 rad/m for K_p. When processed with $n = 4$, the same spectra give an average value of 33.1 for N and 0.1118 rad/m for K_p. These values are remarkably close together, which constitutes a check of the assumption of independence of the 8-time integrated samples. The inferred average value of $N(= 33.6)$ is close, although slightly larger than, the value for independent individual samples ($N = 32$). Since the standard deviation of all the values obtained for N over the four series of radar spectra is as large as 2.0, we adopt the value expected for independent samples, $N = 32$. As for K_p, we take the average value (including the $n = 2$ and $n = 4$ cases), $K_p = 0.112$ rad/m.

References

[1] W. J. Pierson, Jr., "Some approaches for comparing remote and *in-situ* estimates of directional wave spectra," in *Johns Hopkins APL Tech. Dig.,* vol. 8, no. 1, pp. 48–54, 1987.

[2] D. D. Crombie and J. M. Watts, "Observations of coherent backscatter of 2–10 MHz radio surface waves from the sea," *Deep Sea Res.,* vol. 15, pp. 81–87, 1968.

[3] D. E. Barrick and B. J. Lipa, "A compact transportable HF radar system for directional coastal wave field measurements," in *Ocean Wave Climate,* M. D. Earle and A. Malahoff, Eds. New York: Plenum, 1979, pp. 153–209.

[4] D. Atlas, R. C. Beal, R. A. Brown, P. De Mey, R. K. Moore, C. G. Rapley, and S. T. Swift, "Problems and future directions in remote sensing of the oceans and troposphere: a workshop report," *J. Geophys. Res.*, vol. 91, pp. 2525–2548, 1986.

[5] R. C. Beal, Ed., "Measuring ocean waves from space," *Johns Hopkins APL Tech. Dig.*, vol. 8, no. 1, 1987.

[6] O. M. Phillips and K. Hasselmann, *Wave dynamics and radio probing of the ocean surface.* New York: Plenum Publishing, 1986.

[7] F. C. Jackson and D. R. Lyzenga, "Microwave techniques for measuring directional wave spectra," in *Surface Waves and Fluxes,*Geernaert and Plant, Eds. Kluwer Academic Publishers, 1990, pp. 221–264.

[8] F. I. Gonzalez, R. C. Beal, W. E. Brown, P. S. DeLeonibus, J. W. Sherman III, J. F. R. Gower, D. Lichy, D. B. Ross, C. L. Rufenach, and R. A. Shuchman, "Seasat synthetic aperture radar: ocean wave detection capabilities, *Science*, vol. 204, pp. 1418–1421, 1979.

[9] W. R. Alpers, D. B. Ross, and C. L. Rufenach, "On the detectability of ocean surface waves by real and synthetic aperture radar," *J. Geophys. Res.*, vol. 86, pp. 6481–6498, 1981.

[10] W. McLeish and D. B. Ross, "Imaging radar observations of directional properties of ocean waves," *J. Geophys. Res.*, vol. 88, pp. 4407–4419, 1983.

[11] R. C. Beal, D. G. Tilley, and F. M. Monaldo, "Large- and small-scale spatial evolution of digitally processed ocean wave spectra from the Seasat synthetic aperture radar," *J. Geophys. Res.*, vol. 88, pp. 1761–1778, 1983.

[12] R. C. Beal, *et al,* "A comparison of SIR-B directional ocean wave spectra with aircraft scanning radar spectra and global spectral ocean wave model predictions, *Science,* vol. 232, pp. 1531–1535, 1986.

[13] F. M. Monaldo and D. R. Lyzenga, "Comparison of SIR-B ocean wave image spectra with linear model predictions based on aircraft measurements," *J. Geophys. Res.*, vol. 93, pp. 15,374–15,388, 1988.

[14] W. R. Alpers and C. Brüning, "On the relative importance of motion-related contributions to the SAR imaging mechanism of ocean waves," *IEEE Trans. Geosci. Remote Sensing,* vol. GE-24, pp. 873–885, 1986.

[15] F. M. Monaldo and D. R. Lyzenga, "On the estimate of wave slope- and height-variance spectra from the SAR Imagery, *IEEE Trans. Geosci. Remote Sensing,* vol. GE-24, pp. 543–551, 1986.

[16] R. A. Cordey and J. T. Macklin, "Imaging of ocean waves by synthetic aperture radar: a comparison of results from Seasat and SIR-B experiments in the North Atlantic," *IEEE Trans. Geosci. Remote Sensing,* vol. 27, no. 5, pp. 568–575, 1989.

[17] F. M. Monaldo, "A practical methodology for estimating wave spectra from the SIR-B," in *Johns Hopkins APL Tech. Dig.*, vol. 8, no. 1, pp. 82–86, 1987.

[18] E. J. Walsh, D. W. Hanckock, D. E. Hines, R. N. Swift, and J. F. Scott, "Directional Wave spectra measured with the surface contour radar," *J. Phys. Oceanogr.*, vol. 15, pp. 566–592, 1985.

[19] E. J. Walsh, D. W. Hanckock, D. E. Hines, and J. F. Scott, "Elimination of directional wave spectrum contamination from noise in elevation measurements," *J. Oceanic. Eng.*, vol. OE-10, pp. 376–381, 1985.

[20] F. C. Jackson, "An analysis of short pulse and dual frequency radar techniques for measuring ocean wave spectra from satellites," *Radio Sci.*, vol. 16, pp. 1385–1400, 1981.

[21] F. C. Jackson, W. T. Walton, and P. L. Baker, "Aircraft and satellite measurement of ocean wave directional spectra using scanning-beam microwave radars," *J. Geophys. Res.*, vol. 90, pp. 987–1004, 1985.

[22] F. C. Jackson, W. T. Walton, and C. Y. Peng, "A comparison of *in situ* and airborne radar observations of ocean wave directionality," *J. Geophys. Res.*, vol. 90, pp. 1005–1018, 1985.

[23] R. Bernard, D. Vidal-Madjar, F. Baudin, and G. Laurent, "Data processing and calibration for an airborne scatterometer," *IEEE Trans. Geosci. Remote Sensing,* vol. GE-24, pp. 709–716, 1986.

[24] G. R. Valenzuela, "Theories for the interaction of electromagnetic and ocean waves. A review," *Boundary Layer Meteorology,*vol. 13, pp. 61–85, 1978.

[25] G. S. Brown, "Backscattering from a Gaussian-distributed perfectly conducting rough surface," *IEEE Trans. Antennas Propagat.*, vol. AP-26, 3, pp. 472–482, 1978.

[26] H. Masuko, K. Okamoto, M. Shimada, and S. Niwa, "Measurement of microwave backscattering signatures of the ocean surface using X band and $\mathrm{K_u}$ band airborne scatterometers," *J. Geophys. Res.*, vol. 91, no. C11, pp. 13,065–13,083, 1986.

[27] T-I. Bern, "Rehearsal campaign report," *Oceanor Report,* OCN R-90089, 1990.

[28] C. Cox and W. Munk, "Measurement of the roughness of the sea surface from photographs of the sun's glitter," *J. Opt. Soc. Amer.*, vol. 44, no. 11, pp. 838-850, 1954.

Danièle Hauser was born near Grenoble, France in 1955. She received the Ph.D. degree in oceanography and meteorology in 1980, and the Highest Doctorate degree ("Thèse d'Etat") in 1989, from the University "Pierre et Marie Curie," Paris, France.

From 1980 to 1989, she worked at the Centre de Recherches en Physique de l'Environnement (CRPE) at Issy-les Moulineaux, France. Since 1989, she has been a member of the "Remote Sensing" team at CRPE, and is involved in the study of the ocean surface by active microwave sensors. Since 1990, she has been a member of the ESA experimenter team working on the ERS-1 geophysical validation and calibration.

Gérard V. Caudal was born in Lyon, France, on January 27, 1953. He graduated from Ecole Polytechnique in 1974 and Ecole Nationale Supérieure des Télécommunications in 1976.

From 1976 to 1980, he served as an engineer for the operational management of the Telecommunication network in Lille and Lens, France. He then joined the Centre de Recherche en Physique de l'Environnement (CRPE), within the Centre National d'Etudes des Télécommunications (CNET) at Issy-les-Moulineaux and Saint-Maur, France, where he received the Ph.D. degree, with a dissertation on the topic of the electrodynamic coupling between plasma and large-scale electric and magnetic fields in planetary magnetospheres. During 1987–1988, he was a visiting scientist at NASA/Goddard Space Flight Center, Greenbelt, MD, where he performed modeling of the magnetic field in the magnetosphere of Jupiter. Back in France, he became involved in the remote sensing activities of CRPE, where he performs studies related to modeling the microwave backscatter from the ocean surface.

Gert-Jan Rijckenberg, photograph and biography not available at the time of publication of this issue.

Daniel Vidal-Madjar, photograph and biography not available at the time of publication of this issue.

Georges Laurent, photograph and biography not available at the time of publication of this issue.

Philippe Lancelin, photograph and biography not available at the time of publication of this issue.